



HAL
open science

Prediction of the mechanical response of canine humerus to three-point bending using subject-specific finite element modelling

Cédric P. Laurent, Béatrice Böhme, Marlène Mengoni, Vinciane d'Otreppe,
Marc Balligand, Jean-Philippe Ponthot

► To cite this version:

Cédric P. Laurent, Béatrice Böhme, Marlène Mengoni, Vinciane d'Otreppe, Marc Balligand, et al.. Prediction of the mechanical response of canine humerus to three-point bending using subject-specific finite element modelling. *Proceedings of the Institution of Mechanical Engineers, Part H: Journal of Engineering in Medicine*, 2016, 230 (7), pp.639 - 649. 10.1177/0954411916644269 . hal-01416475

HAL Id: hal-01416475

<https://hal.univ-lorraine.fr/hal-01416475>

Submitted on 27 Mar 2019

HAL is a multi-disciplinary open access archive for the deposit and dissemination of scientific research documents, whether they are published or not. The documents may come from teaching and research institutions in France or abroad, or from public or private research centers.

L'archive ouverte pluridisciplinaire **HAL**, est destinée au dépôt et à la diffusion de documents scientifiques de niveau recherche, publiés ou non, émanant des établissements d'enseignement et de recherche français ou étrangers, des laboratoires publics ou privés.

Prediction of the mechanical response of canine humerus to three-point bending using subject-specific finite element modelling

Cédric P. Laurent^{1,2}, Béatrice Böhme³, Marlène Mengoni^{1,4}, Vinciane d'Otreppe¹, Marc Balligand³, Jean-Philippe Ponthot¹

1 University of Liege, Department of Aerospace and Mechanical Engineering, Belgium

2 CNRS, LEMTA, UMR 7563, Université de Lorraine, France

3 University of Liege, Department of Clinical Sciences, College of Veterinary Medicine, Belgium

4 Institute of Medical and Biological Engineering, School of Mechanical Engineering, University of Leeds, UK

Corresponding author:

Cédric P. Laurent, CNRS, LEMTA, UMR 7563, Université de Lorraine, 2 avenue de la forêt de Haye, F-54502 Vandoeuvre-lès-Nancy, France

Email: Cedric.laurent@univ-lorraine.fr

Submitted as an original article

Word count: 3874 (max 5000)

Abstract

Subject-specific finite element (FE) models could improve decision making in canine long bone fracture repair. However, it preliminary requires that FE models predicting the mechanical response of canine long bone are proposed and validated. We present here a combined experimental-numerical approach to test the ability of subject-specific FE models to predict the bending response of seven pairs of canine humeri directly from medical images. Our results show that bending stiffness and yield load are predicted with a mean absolute error of 10.1% ($\pm 5.2\%$) for the fourteen samples. This study constitutes a basis for the forthcoming optimization of canine long bone fracture repair.

Keywords

Finite element modelling

Subject-specific

Canine bone material properties

Bending test

Canine humerus

1 Introduction

2 Long bone fracture constitutes a common reason for medical consultation within
3 veterinary orthopaedic services^{1,2}, as emphasized by the substantial recent literature
4 concerning the choice of adapted implants³⁻⁶. Associated surgical interventions are
5 often complex given that each fracture has its own particularities. Canine bone fracture
6 repair differs from the human case in the sense that (1) the physiological characteristics
7 and morphology of the injured bones in animals vary considerably⁷, (2) the animal is not
8 able to limit its activity during the post-operative period, which may lead to premature
9 overloading, and (3) the surgeon is often confronted to cost limitations concerning
10 orthopaedic material. As a result, the treatment of such fractures (implant type,
11 dimension, location ...) depends to some extent on the surgeon's experience, who tries
12 to find a trade-off between a minimum stiffness required for fracture stabilization and
13 a sufficient flexibility essential for bone remodelling. Although available handbooks
14 guide the surgeon in the choice of a suited treatment for each particular fracture, they
15 are still based on empirical knowledge, and there is a lack of studies assessing the effect
16 of different treatment types on the biomechanical properties of the reconstructed bone.
17 This insufficient knowledge may partly explain the complications that are still frequent
18 in the field of canine fracture repair^{8,9}.

19 In order to improve the surgical procedure, ex-vivo experiments^{10,11} as well as numerical
20 biomechanical studies¹²⁻¹⁴ have been reported. Indeed, numerical approaches, such as
21 Finite Element (FE) modelling may enable to evaluate non-invasively the effect of
22 various implants or their combination on the same bone sample. However, these FE
23 studies are often based on simplistic bone models (i.e. elastic, linear, homogeneous
24 cortical and trabecular tissues, etc...). A milestone in delivering relevant data in a
25 subject-specific approach consists of including the bone external geometry and
26 heterogeneous material properties from the information available in CT images. Such
27 subject-specific FE approaches have been developed in human long bone analysis and
28 satisfyingly predicted the failure risk in proximal femur¹⁵⁻¹⁸. However, available studies
29 in human have often led to moderately accurate results as far as the prediction of the
30 global biomechanical response of long bones are concerned, probably due to
31 accumulating inherent approximations throughout the model generation. Particularly,
32 it is not clear if the consideration of density-dependent material properties leads to
33 better results than the modelling of long bone with two materials (trabecular and
34 cortical tissues) separated from a density criterion. The interest of considering
35 anisotropic material properties is also not clear. Moreover, if one wants to extend these
36 subject-specific FE models to canine bone, a supplementary difficulty will come from the
37 variability of bone material properties from one breed to another¹⁹, and from the

38 absence of data concerning relationships between CT information and bone material
39 properties for dogs.

40 Such FE models are usually validated using *ex vivo* mechanical tests such as bending^{20,21},
41 torsion²² or compression^{17,23}. These combined experimental-numerical approaches
42 require that a particular attention is paid to the application of similar Boundary
43 Conditions (BC), such as load application and displacement restriction, in the
44 experimental and computational setups²⁴.

45 In the present contribution, the hypothesis was that subject-specific FE models are able
46 to predict the global mechanical response of canine long bones to three-point bending
47 tests. The aims of the present work were therefore (1) to provide a direct subject-
48 specific validation of canine long bone FE models including a novel density-elasticity law;
49 and (2) to assess the requirements for the bone material model to replicate measured
50 *ex vivo* behaviour.

51 **Material and Methods**

52 A combined experimental and computational approach was developed to validate the
53 FE models with *ex vivo* three-point bending data, i.e. overall load/deflection behaviour
54 and local fracture patterns. All dynamic FE analyses were performed using the in house
55 non-linear implicit FE code MetaFor (metafor.ltas.ulg.ac.be).

56 *Specimen preparation, imaging, and mechanical testing*

57 Eight pairs of canine humeri were initially harvested from adult dogs euthanized for
58 reasons unrelated to this study. After harvesting, one dog (i.e. one pair of humeri) was
59 excluded from this study due to the observation of severe knee arthrosis. Dog weights
60 finally ranged from 19 to 39kg. Soft tissues were carefully removed and samples were
61 wrapped in saline soaked sponges and stored at -20°C. Samples were prepared for
62 three-point bending mechanical tests at room temperature. In order to accurately
63 control the location of the bones within the custom bending stand and to restrict
64 rotations around the bone diaphysis axis during the bending tests, the epiphyses were
65 embedded into 60×60×60mm³ moulds made of two-component polymeric resin
66 (Motip®, Germany) (Figure 1). A particular attention was paid to define resin moulds
67 orientation with respect to the bone sample position in a reproducible way. Firstly, we
68 used the origin of the medial and lateral collateral ligaments as anatomical landmarks
69 to define a reference axis. Then, the distal resin mould was created in such a way that
70 this anatomical reference axis was parallel to two surfaces of the resin block (namely its
71 cranio-caudal and proximal-distal surfaces). The second mould was perfectly aligned
72 with the first one, using custom-made jig (Figure 1.a).

73 The samples were imaged using a CT-scanner (Siemens SOMATOM at 120 kVp) with a
74 slice thickness of 0.75mm and a spatial resolution of 0.1445mm. A phantom (Siemens

75 BMD calibration phantom²⁵) was used to calibrate the bone densities with respect to
76 the Hounsfield Units (HU) issued from the CT acquisition^{18,26}. Particular attention was
77 paid to keep the samples packed in saline-soaked wraps throughout the procedure in
78 order to avoid tissue dehydration. The following relation was obtained:

79
$$\rho = 4.9332 \cdot 10^{-4} HU + 0.9839 (1)$$

80 Samples were placed on a custom adjustable bending stand (Figure 1.b) made of two
81 steel half-cylinders. The cylinders positions were adjusted so that they were in contact
82 with the middle of each resin mould in the axial direction of the bone. The bending tool
83 consisted in a cylindrical punch located longitudinally at half the distance between the
84 two resin moulds. The stand was mounted in a 100 kN servo-hydraulic testing machine
85 (Zwick/Roell, Ulm, Germany, load cell : XForce HP 5 kN). A medial-lateral displacement
86 was applied to the bending tool at a speed of 0.2 mm.s⁻¹ after a preload of 50 N. The
87 samples were tested until complete fracture. Tool displacement (hereafter called
88 deflection) and vertical force (i.e. shear force) were recorded. Two high speed cameras
89 (Vision Research v7.3) recording 1000 frames/s were used in order to visualize the
90 fracture onset.

91 *Finite Element modelling*

92 Each tested sample was modelled with a subject-specific approach. The geometry of the
93 bone were built from the 3D CT data using 3D-Slicer²⁷ (www.slicer.org) for segmentation
94 and a dedicated in-house algorithm²⁸ for the generation of smooth multi-region surface
95 meshes. The bone volume mesh was obtained using Tetgen (WIAS, Berlin, Germany),
96 generating linear tetrahedra. Final mesh size was issued from a mesh dependency
97 analysis reported hereafter.

98 The resin moulds were not meshed in the FE model but considered as single deformable
99 hexahedrons whose coordinates were automatically computed from the boundaries of
100 resin moulds in the surface mesh (Figure 1.b). Resin was considered linear elastic, with
101 an elastic modulus of 900 MPa characterized from preliminary experiments. Elements
102 were assigned a density issued from the calibration phantom, and equal to $1\text{g}\cdot\text{cm}^{-3}$ for
103 resin. The interaction between the bone and the resin moulds was modelled using
104 springs (arbitrary stiffness of 100 N mm^{-1}) linking the hexahedron nodes with each of
105 the bone surface nodes located within the resin moulds (Figure 1.b) in order to constrain
106 the relative displacement between bone and resin. This numerical representation of the
107 resin blocks is totally equivalent to a penalty formulation in contact algorithms with
108 bilateral restrictions to enforce the continuity of the displacement field at the interface

109 between bone and resin. The proximal resin mould was restrained in the cranio-caudal
110 direction.

111 The bending stand was modelled as two rigid half-cylinders located longitudinally at the
112 middle of each resin moulds. The frictional contact condition between the resin moulds
113 and the bending stand was modelled with a Coulomb's law, with static and dynamic
114 friction coefficients set at 0.7, corresponding to a dry static contact between steel and
115 steel²⁹. This value was chosen due to the lack of published value for resin-steel contact.
116 Each half-cylinders of the bending stand were restrained in their 6 degrees of freedom.

117 The bending tool was modelled as a rigid half-cylinder located, as marked
118 experimentally, at half the distance between the two resin moulds. Displacement was
119 applied to the tool in the medial-lateral direction. Contact between the bending tool and
120 the bone surface was modelled as sticking contact.

121 A sensitivity analysis was performed analysing the effect of the resin properties, the
122 stiffness of the springs used to attach bone to resin blocks and the friction coefficient
123 between resin and stand on the predicted bone stiffness and yield load. Load-deflection
124 curves were obtained as the sum of the medial-lateral component of the contact force
125 and the tool displacement at each time step. The experimental preload was mimicked
126 by excluding the initial forces below 50N from the simulation results.

127 For each sample, user interaction was only needed for the image segmentation step. To
128 avoid user variation, all other steps of the model creation and analysis were automated,
129 based on the size of the samples extracted from the segmented data. All FE analyses
130 were performed using local HPC facilities (parallel computation on 144 cores).

131 *Bone material models*

132 Three different materials models were considered for the bone: a density-dependent
133 transversely isotropic model, a density-dependent isotropic model, and a two-material
134 isotropic model (one material model for cortical bone and one for trabecular bone).

135 For the density dependent models, material parameters were mapped against the HU
136 values from the CT scans starting from equation (1). The following mapping procedure
137 was applied: (1) for each mesh element, the smallest rectangular box that embraced the
138 tetrahedron was defined, (2) for each voxel included within this box, material properties
139 (see next section) were computed from the density computed from the HU field, and (3)
140 material properties were averaged on this box and assigned to the mesh element. A
141 particular attention was paid to reduce the partial volume artefacts: to this end, we
142 firstly separated the mesh elements that had at least one point belonging to the bone
143 surface (*outer cells*) from the other mesh elements (*inner cells*). Each outer cell was then
144 associated to its closest inner cell, and was assigned the HU value of its associated inner

145 cell when it was higher than its own HU value. This procedure significantly reduced the
146 partial volume artefact, provided that the bone cortical wall was described by a
147 sufficient number of mesh elements, i.e. that the mesh was sufficiently dense.

148 It is known that the properties of canine bone depends on dog mass¹⁹. Therefore a
149 density-elasticity relationship had to be derived for canine bone. It would indeed not be
150 justified to use a unique density-elasticity relationship determined from human bone.
151 Published experimental data¹⁹ reported the elastic moduli of canine cortical bone as a
152 function of dog breed: 13.3GPa (dog mass=5kg), 14.9GPa (dog mass=12kg), 16GPa (dog
153 mass=25kg), 16.3GPa (dog mass=50kg). Comparing that data to an average reported
154 elastic modulus of 17.9GPa for human cortical bone³⁰, the following relation between
155 human data and canine data was extrapolated (using a common mean-square method):

$$156 \quad E_{\text{canine}}(\rho) = E_{\text{human}}(\rho) \times (0.3 \exp(-5/m) + 0.64) \quad (2)$$

157 by denoting m the dog mass. This relation is illustrated on Figure 2, and assumes that
158 bone properties depend only on dog mass and not on the breed.

159 This canine-to-human relation was used to weight existing density-elasticity
160 relationships validated for human data:

161 For the density-dependent transversely isotropic model, bone was considered as an
162 elastoplastic material without distinction between cortical and trabecular tissues

163 (except for density). The elastic part of the model was built from relation (2) and using
164 an orthotropic elasticity-density relationship for human bone in tension³¹:

$$\begin{aligned} E_l &= 2065\rho^{3.09} & G_{lt} &= 0.29E_l \\ E_t &= 2314\rho^{1.57} & G_{tt} &= 0.2E_l \end{aligned} \quad (3)$$

166 by denoting E_l and E_t the elastic moduli (MPa) in the longitudinal and transverse
167 directions, G_{lt} and G_{tt} the shear moduli (MPa), and ρ (g cm^{-3}) the apparent density issued
168 from CT calibration. These relations valid for human bone were weighted using relation
169 (2) in order to model canine bone. Asymmetric elastic material properties were assumed
170 by considering that the elastic modulus was 6% higher in compression than in tension³².

171 The global longitudinal direction was automatically computed for each sample, based
172 only on the central third of the bone (representing the diaphysis, see Figure 3). The mesh
173 nodes belonging to the bone surface and included in this part were selected, and used
174 to compute a least-square line defined as the longitudinal direction. The transverse
175 direction was defined perpendicularly to this direction, in a plane containing the tool
176 displacement vector.

177 The yield surface was defined through a Von Mises criterion with linear isotropic
178 hardening. The initial yield stress was obtained from the yield strain of 0.73% reported

179 for human cortical bone³³ and the mean elastic modulus (defined as the average of
180 longitudinal and transverse moduli) following the relation:

$$181 \quad \sigma_y = 0.0073(E_l + E_t) / 2 \quad (4)$$

182 The role of the longitudinal stress was therefore considered predominant in the bone
183 yield. Post-yield hardening was set as 5% of the initial, density-dependent, mean elastic
184 moduli³⁴.

185 The same procedure was applied for the density-dependent isotropic model. The unique
186 Young modulus was defined as the mean of the computed longitudinal and transverse
187 modulus for a given bone density (relation (3)) weighted by the correction coefficients
188 given in relation (2). Yield was modelled identically to the previous model.

189 For the two-material isotropic model, trabecular and cortical canine tissues were
190 respectively modelled with Young's modulus of 750MPa and 15GPa and a Poisson's ratio
191 of 0.3³⁵. Cortical and trabecular tissues were separated using a threshold in terms of HU
192 values. Cortical tissue was assumed for HU values superior to either 600HU or 400HU in
193 order to assess the sensitivity to this parameter. Yield was modelled identically to the
194 previous models.

195 *Statistical analysis*

196 For each tested bone, bending stiffness (least-square linear regression of the linear part
197 of force-deflection curve passing through the origin) and yield load (intersection
198 between a parallel to this linear regression with a 0.1 mm offset and the force-deflection
199 curve) were extracted and compared between the experimental and computational
200 data.

201 In order to emphasize the statistical significance of our model, we performed various
202 statistical analyses from our experimental results (14 samples from 7 dogs) and our
203 numerical results (56 models: 14 density-dependant transversely isotropic models, 14
204 density-dependant isotropic models, and 14 two-materials isotropic models with a
205 segmentation threshold of 400 HU or 600 HU). Analysis of variance (ANOVA) was used
206 as the common test to quantify the difference between two sets of data, with a default
207 p-value of 0.01 (when not detailed).

208 **Results**

209 *Experimental results*

210 Experimental results for the seven pairs of humeri are represented in Figure 4. A large
211 intra- and inter-variability was observed: as an example, a mean difference of 14.6% in
212 stiffness between the left and right humerus of the same dog. Left and right humerus of

213 the same dog were however not different (both in terms of stiffness and yield load) in
214 the sense of an ANOVA analysis. The coefficient of variation (ratio between standard
215 deviation and mean) of the stiffness is equal to 20.2%. The data showed a weak
216 correlation between dog mass and mean humerus stiffness (correlation coefficient of
217 0.65). While the failure was sudden for six samples, it was more progressive for the
218 others and no clear fracture pattern was therefore visible.

219 *Computational results*

220 The meshes resulting from the reconstruction of the segmented CT images together
221 with the mapping procedure are represented in Figure 5 for all bone samples. Bone
222 mesh made of approximately 300 000 tetrahedral linear elements (60 000 nodes) led to
223 a relative difference of 2.5% on strain energy density (SED) and 1.4% on stiffness
224 compared to the values obtained for 160 000 nodes. The results of the sensitivity study
225 for one humerus are reported in Table 1. These data emphasize that the simulation
226 results are not sensitive to resin properties, indicating that the resin does not deform
227 substantially during the bending test. Moreover, the simulation results are very slightly
228 sensitive to the stiffness of springs used to attach bone to resin (2% of deviation for a
229 variation of five orders of magnitude). A stiffness of 100N/mm (i.e. of the same order of
230 magnitude than the bone bending stiffness) has been consequently selected for every
231 simulations. However, this sensitivity study emphasizes that the friction coefficient does

232 have an effect on predicted stiffness and yield load. A friction coefficient of 0.7 has been
233 chosen for the simulations due to the lack of existing data, as long as such data are
234 difficult to measure experimentally.

235 For the density-dependent transversely isotropic model on the fourteen samples, the
236 bending stiffness was predicted with a maximum error of 21.7% (absolute value of the
237 mean error = $10.1\% \pm 5.2\%$). The yield load was predicted with an absolute value of the
238 mean error $11\% \pm 11.3\%$, but was unsatisfyingly predicted for one sample over the
239 fourteen samples (maximum error = 43.5%, see Figure 6). Correlation coefficients
240 between predicted and measured values were 0.86 for stiffness and 0.74 for yield load.

241 A Bland-Altman representation of the simulation results obtained with this model has
242 also been provided (Figure 7) : it clearly illustrates the good prediction ability of this
243 model. However, this representation clearly emphasizes that the values of bending
244 stiffness and yield load are badly predicted for one sample (#6 right).

245 Results of the different models were confronted to experimental results in the sense of
246 ANOVA statistical tests, and the *p-values* issued from these tests are gathered in Table
247 2, under the null hypothesis that experimental and simulations results have the same
248 mean (i.e. if the *p-value* is near to zero, experimental and simulation results are
249 significantly different). From this analysis, it is clear that the density-dependant
250 transversely isotropic model is the most predictive model among the four different

251 models tested, and especially compared to the density-dependant isotropic model, as
252 illustrated on Figure 8. Surprisingly, the computational results are better in the case of
253 the two-material isotropic models (no matter the segmentation threshold) than in the
254 case of density-dependant isotropic models.

255 Results of the FE simulations for the two-material isotropic model are represented in
256 Figure 9, with trabecular and cortical tissues being separated either from HU values of
257 400 or 600HU in order to quantify the sensitivity of the bending response to this
258 threshold. There is no statistical difference between the two threshold values used to
259 separate cortical from trabecular tissue in the case of two-material models.

260 **Discussion**

261 *Model accuracy*

262 A finite element mesh of 60 000 nodes showed to be a converged mesh for the bone
263 stiffness and strain energy density (SED). A satisfying prediction of bone stiffness was
264 obtained for every samples, whereas the yield load was satisfyingly predicted for 13 over
265 14 samples. The reported computational results were insensitive to the properties
266 assigned to the resin block holding the bone epiphysis; this indicates that resin blocks
267 do not deform much during the simulations. The computational representation of those

268 blocks is thus a good approximation of the blocks behaviour and interaction with the
269 bone.

270 Using the verified and validated non-linear FE software Metafor³⁶⁻³⁹ to analyse long
271 bone three-point bending tests permits high automation of the model pre- and post-
272 processing steps. This reduces user-variability to the image segmentation step only. All
273 other parameters, especially as far as the definition of model boundary conditions
274 representative of the experimental conditions is concerned, are subject only to the
275 experimental variability.

276 Density-elasticity relationships for canine long bone as a function of dog mass were
277 determined by weighting human relationships from published canine bone properties.
278 Using material parameters from literature only, and not specifically calibrated on the
279 experimental results, the produced models were able to satisfyingly predict bending
280 stiffness and yield load. However, more detailed studies on microstructure or
281 composition of canine bone as a function of mass (or breed) would be required in order
282 to propose a more comprehensive relation.

283 The predictive power of the models for stiffness values and yield loads is here reflected
284 not only by a good correlation but also by a good concordance, which is less often the
285 case in published models^{40,41}. This therefore suggested that the approach used in this

286 work produces valid models to predict bone stiffness and yield loads in three-point
287 bending of canine long bones.

288 *Comparison between models*

289 The benefit of the non-linear density-dependent transversely isotropic model compared
290 to the two other models is demonstrated in terms of its improved prediction capability.
291 However, it is surprising that the two-material isotropic model leads to better
292 predictions than the density-dependent isotropic model. This may be explained by the
293 fact that, during a bending test, the bone is essentially subject to tension and
294 compression, and therefore the longitudinal modulus of the bone plays a crucial role
295 compared to transverse modulus. In the case of the density-dependant isotropic model,
296 the computed average Young modulus is therefore underestimated, for a loading
297 involving mainly the longitudinal direction. Predicted stiffness is thus globally
298 underestimated using the density-dependant isotropic model. On the contrary, the two-
299 material model may widely overestimate the Young modulus by considering constant
300 density for cortical bone, as it is clearly seen that it is not uniform over the cortical bone
301 (Figure 5). Therefore, , it may lead to higher errors in more complex loading modes even
302 without involving a huge overestimation of bone properties in the case of bending loads.
303 For instance, a HU value of 1500HU for cortical bone corresponds to longitudinal and
304 transverse moduli of 9.7GPa and 4.7GPa respectively using the density-dependant

305 transversely isotropic model, whereas it corresponds to a Young modulus equal to
306 7.2GPa using the density-dependant isotropic model, and equal to 15GPa in the case of
307 the two-material models. One other limitation of the two-material model is the
308 sensitivity of the results to the threshold value chosen to separate trabecular and
309 cortical tissues, which may be user-dependent. This limit obviously disappears when the
310 density-dependent model is used.

311 As far as the ease of implementation is concerned, computation times were equivalent
312 for the three models. However, density-dependant models require to develop and
313 algorithm in order to link HU values to elastic properties, and also require a calibration
314 of the CT-scan. Moreover, using a transversely isotropic model requires the definition of
315 orthotropic axis, which has been approximated in our case for bending tests. More
316 complex algorithms would be required to assign local orthotropic axis for more complex
317 loadings. Except for these pre-processing steps, the calculation of the three types of
318 models is then straightforward.

319 *Limitations and challenges*

320 One of the limitation of bending tests lies in the fact that results depend on the friction
321 coefficient between sample and the bending tools, as illustrated by our sensitivity
322 analysis and by other authors ⁴². Bending stand–resin interaction was modelled with

323 friction coefficient of 0.7 due to the lack of existing values. Even if this friction coefficient
324 is realistic for such a soft resin, experiments could be performed in order to confirm
325 these results. However, such measurements are complex to perform, as long as
326 apparent friction coefficients may be affected by local deformation of the resin due to
327 the cylindrical shape of the bending stand and the high loads involved. These local
328 effects are not taken into account in the simulations, as long as resin blocks have been
329 modelled by a single element. This particular point may be subject to further analyses,
330 for instance using an inverse approach from similar bending tests on well-known
331 materials.

332 A simple elastoplastic law with isotropic linear hardening was used as proposed in the
333 literature³³, and associated with a Von Mises yield criterion. Even though the use of such
334 a criterion has been questioned⁴³, no consensus has been clearly found and this criterion
335 is still widely used^{34,38,40}. The simulated post-yield response did not reproduce the
336 plateau observed experimentally for some samples: it may be therefore concluded that
337 the linear hardening set as 5% of the initial mean modulus as proposed in the literature
338 was excessive and should be age and breed dependent, or that a perfectly plastic
339 behaviour might be more representative. Including progressive damage in the model
340 may lead to better results as the physical phenomenon leading to bone non-linear
341 behaviour is most probably related to damage rather than plasticity^{21,34,38,44}.

342 No distinction was made between cortical and trabecular tissues in the bone material
343 properties characterising the non-linear behaviour, although the microstructures of
344 these tissues are clearly different. It is likely that here the trabecular tissue do not
345 participate substantially to the bone bending response. The material axes were defined
346 from the mid-line of the diaphysis, as commonly reported in the literature^{45,46}, leading
347 to a global definition of the longitudinal direction. As the segment of interest involved
348 in the bending test was restricted to the bone diaphysis in which the main orthotropic
349 direction does not substantially vary, it is unlikely that this simplification has an effect
350 on the reported results. These two limitations suggest that the validity of the procedure
351 proposed here is thus probably restricted to the bending mode of deformation.

352 **Acknowledgements**

353 The authors would like to acknowledge the Research Council of the University of Liège
354 for having selected this research in their funding program.

355 **Conflicts of interest**

356 There is no conflict of interest in this study.

357 **References**

- 358 1. Kumar, K. *et al.* Occurrence and Pattern of Long Bone Fractures in Growing Dogs
359 with Normal and Osteopenic Bones. *J. Vet. Med. Ser. A* **54**, 484–490 (2007).
- 360 2. Miller, C. W., Sumner-Smith, G., Sheridan, C. & Pennock, P. W. Using the Unger
361 system to classify 386 long bone fractures in dogs. *J. Small Anim. Pract.* **39**, 390–393
362 (1998).
- 363 3. Voss, K., Kull, M. A., Hässig, M. & Montavon, P. M. Repair of long-bone fractures in
364 cats and small dogs with the Unilock mandible locking plate system. *Vet. Comp.*
365 *Orthop. Traumatol.* **5**, 398–405 (2009).
- 366 4. Ayyappan, S., Shafiuzama, M., Ganesh, T. N., Das, B. C. & Kumar, R. . A clinical study
367 on external fixators for long bone fracture management in dogs. *Indian J. Vet. Surg.*
368 **30**, 90–92 (2009).
- 369 5. Rahal, C., Otoni, C., Pereira, O., Blum, A. & Vulcano, L. Synthesis Pengo System plates
370 for the treatment of long-bone diaphyseal fractures in dogs. *Vet. Comp. Orthop.*
371 *Traumatol. VCOT* **21**, 59–63 (2008).
- 372 6. Dueland, R., Johnson, K., Roe, S., Engen, M. & Lesser, A. Interlocking nail treatment
373 of diaphyseal long-bone fractures in dogs. *J. Am. Vet. Med. Assoc.* **214**, 59–66 (1999).

- 374 7. Palierne, S., Asimus, E., Mathon, D., Meynaud-Collard, P. & Autefage, A. Geometric
375 analysis of the proximal femur in a diverse sample of dogs. *Res. Vet. Sci.* **80**, 243–
376 252 (2006).
- 377 8. Dvořák, M., Nečas, A. & Zatloukal, J. Complications of Long Bone Fracture Healing in
378 Dogs: Functional and Radiological Criteria for their Assessment. *Acta Vet. Brno* **69**,
379 107–114 (2000).
- 380 9. Jackson, L. C. & Pacchiana, P. D. Common complications of fracture repair. *Clin. Tech.*
381 *Small Anim. Pract.* **19**, 168–179 (2004).
- 382 10. Blake, C. A. *et al.* Single cycle to failure in bending of three standard and five locking
383 plates and plate constructs. *Vet. Comp. Orthop. Traumatol. VCOT* **24**, 408–417
384 (2011).
- 385 11. Zahn, K. *et al.* Mechanical properties of 18 different AO bone plates and the clamp-
386 rod internal fixation system tested on a gap model construct. *Vet. Comp. Orthop.*
387 *Traumatol.* **21**, 185–194 (2008).
- 388 12. Nassiri, M., MacDonald, B. & O’Byrne, J. M. Locking compression plate breakage and
389 fracture non-union: a finite element study of three patient-specific cases. *Eur. J.*
390 *Orthop. Surg. Traumatol.* **22**, 275–281 (2012).
- 391 13. Oh, J.-K. *et al.* Effect of fracture gap on stability of compression plate fixation: A finite
392 element study. *J. Orthop. Res.* **28**, 462–467 (2010).

- 393 14. Vajgel, A. *et al.* Comparative Finite Element Analysis of the Biomechanical Stability
394 of 2.0 Fixation Plates in Atrophic Mandibular Fractures. *J. Oral Maxillofac. Surg.* **71**,
395 335–342 (2013).
- 396 15. Bessho, M. *et al.* Prediction of proximal femur strength using a CT-based nonlinear
397 finite element method: Differences in predicted fracture load and site with changing
398 load and boundary conditions. *Bone* **45**, 226–231 (2009).
- 399 16. Hambli, R., Bettamer, A. & Allaoui, S. Finite element prediction of proximal femur
400 fracture pattern based on orthotropic behaviour law coupled to quasi-brittle
401 damage. *Med. Eng. Phys.* **34**, 202–210 (2012).
- 402 17. Tsouknidas, A., Anagnostidis, K., Maliaris, G. & Michailidis, N. Fracture risk in the
403 femoral hip region: A finite element analysis supported experimental approach. *J.*
404 *Biomech.* **45**, 1959–1964 (2012).
- 405 18. Hambli, R. & Allaoui, S. A Robust 3D Finite Element Simulation of Human Proximal
406 Femur Progressive Fracture Under Stance Load with Experimental Validation. *Ann.*
407 *Biomed. Eng.* **41**, 2515–2527 (2013).
- 408 19. Autefage, A., Palierne, S., Charron, C. & Swider, P. Effective mechanical properties
409 of diaphyseal cortical bone in the canine femur. *Vet. J.* **194**, 202–209 (2012).
- 410 20. Duprey, S., Bruyere, K. & Verriest, J.-P. Experimental and simulated flexion tests of
411 humerus. *Int. J. Crashworthiness* **12**, 153–158 (2007).

- 412 21. Hambli, R. & Thurner, P. J. Finite element prediction with experimental validation of
413 damage distribution in single trabeculae during three-point bending tests. *J. Mech.*
414 *Behav. Biomed. Mater.* **27**, 94–106 (2013).
- 415 22. Varghese, B., Short, D., Penmetsa, R., Goswami, T. & Hangartner, T. Computed-
416 tomography-based finite-element models of long bones can accurately capture
417 strain response to bending and torsion. *J. Biomech.* **44**, 1374–1379 (2011).
- 418 23. Trabelsi, N., Yosibash, Z., Wutte, C., Augat, P. & Eberle, S. Patient-specific finite
419 element analysis of the human femur: a double-blinded biomechanical validation. *J.*
420 *Biomech.* **44**, 1666–1672 (2011).
- 421 24. Viceconti, M., Olsen, S., Nolte, L.-P. & Burton, K. Extracting clinically relevant data
422 from finite element simulations. *Clin. Biomech. Bristol Avon* **20**, 451–454 (2005).
- 423 25. Kalender, W. A. & Suess, C. A new calibration phantom for quantitative computed
424 tomography. *Med. Phys.* **14**, 863–866 (1987).
- 425 26. Austman, R. L., Milner, J. S., Holdsworth, D. W. & Dunning, C. E. The effect of the
426 density–modulus relationship selected to apply material properties in a finite
427 element model of long bone. *J. Biomech.* **41**, 3171–3176 (2008).
- 428 27. Fedorov, A. *et al.* 3D Slicer as an image computing platform for the Quantitative
429 Imaging Network. *Magn. Reson. Imaging* **30**, 1323–1341 (2012).

- 430 28. d’Otreppe, V., Boman, R. & Ponthot, J.-P. Generating smooth surface meshes from
431 multi-region medical images. *Int. J. Numer. Methods Biomed. Eng.* **28**, 642–660
432 (2012).
- 433 29. Sullivan, J. F. in *Technical Physics* (Wiley, 1988).
- 434 30. Reilly, D. T. & Burstein, A. H. The elastic and ultimate properties of compact bone
435 tissue. *J. Biomech.* **8**, 393–405 (1975).
- 436 31. Wirtz, D. C. *et al.* Critical evaluation of known bone material properties to realize
437 anisotropic FE-simulation of the proximal femur. *J. Biomech.* **33**, 1325–1330 (2000).
- 438 32. Li, S., Demirci, E. & Silberschmidt, V. V. Variability and anisotropy of mechanical
439 behavior of cortical bone in tension and compression. *J. Mech. Behav. Biomed.*
440 *Mater.* **21**, 109–120 (2013).
- 441 33. Bayraktar, H. H. *et al.* Comparison of the elastic and yield properties of human
442 femoral trabecular and cortical bone tissue. *J. Biomech.* **37**, 27–35 (2004).
- 443 34. Verhulp, E., van Rietbergen, B. & Huiskes, R. Load distribution in the healthy and
444 osteoporotic human proximal femur during a fall to the side. *Bone* **42**, 30–35 (2008).
- 445 35. Verim, O., Tasgetiren, S., Er, M. S., Ozdemir, V. & Yuran, A. F. Anatomical evaluation
446 and stress distribution of intact canine femur. *Int. J. Med. Robot.* **9**, 103–108 (2013).
- 447 36. Boman, R. & Ponthot, J.-P. Efficient ALE mesh management for 3D quasi-Eulerian
448 problems. *Int. J. Numer. Methods Eng.* **92**, 857–890 (2012).

- 449 37. Jeunechamps, P.-P. & Ponthot, J.-P. An efficient 3D implicit approach for the
450 thermomechanical simulation of elastic–viscoplastic materials submitted to
451 high strain rate and damage. *Int. J. Numer. Methods Eng.* **94**, 920–960 (2013).
- 452 38. Mengoni, M. & Ponthot, J. P. A generic anisotropic continuum damage model
453 integration scheme adaptable to both ductile damage and biological damage-like
454 situations. *Int. J. Plast.* **66**, 46–70 (2015).
- 455 39. Mengoni, M. *et al.* A non-linear homogeneous model for bone-like materials under
456 compressive load. *Int. J. Numer. Methods Biomed. Eng.* **28**, 273–287 (2012).
- 457 40. Helgason, B. *et al.* A modified method for assigning material properties to FE models
458 of bones. *Med. Eng. Phys.* **30**, 444–453 (2008).
- 459 41. Taddei, F., Schileo, E., Helgason, B., Cristofolini, L. & Viceconti, M. The material
460 mapping strategy influences the accuracy of CT-based finite element models of
461 bones: an evaluation against experimental measurements. *Med. Eng. Phys.* **29**, 973–
462 979 (2007).
- 463 42. Zeng, X., Wen, S., Li, M. & Xie, G. Estimating Young’s Modulus of Materials by a New
464 Three-Point Bending Method. *Adv. Mater. Sci. Eng.* **2014**, e189423 (2014).
- 465 43. Doblaré, M., García, J. M. & Gómez, M. J. Modelling bone tissue fracture and healing:
466 a review. *Eng. Fract. Mech.* **71**, 1809–1840 (2004).

- 467 44. Burkhart, T. A., Quenneville, C. E., Dunning, C. E. & Andrews, D. M. Development and
468 validation of a distal radius finite element model to simulate impact loading
469 indicative of a forward fall. *Proc. Inst. Mech. Eng. [H]* **228**, 258–271 (2014).
- 470 45. Peng, L., Bai, J., Zeng, X. & Zhou, Y. Comparison of isotropic and orthotropic material
471 property assignments on femoral finite element models under two loading
472 conditions. *Med. Eng. Phys.* **28**, 227–233 (2006).
- 473 46. Yang, H., Ma, X. & Guo, T. Some factors that affect the comparison between isotropic
474 and orthotropic inhomogeneous finite element material models of femur. *Med. Eng.*
475 *Phys.* **32**, 553–560 (2010).
- 476
- 477

478 **Figure captions**

479 Figure 1. Experimental and simulated bending test on canine humerus. (a) Preparation
480 of bone samples using a custom jig to align resin moulds (b) bone samples embedded in
481 resin moulds were mounted in a custom bending stand (c) the bending tests were
482 simulated by simplifying the resin moulds with single hexahedrons linked to the bone
483 surface (red dots) via artificial springs. A sticking contact condition was considered
484 between the bending tool and the bone surface (green dots), while contact-friction
485 interaction was considered between the resin moulds and the bending stand (blue
486 cylinders).

487 Figure 2. Determined relation between canine bone properties as a function of mass
488 based on existing data¹⁹ and human bone properties.

489 Figure 3. Calculation of orthotropic axes (longitudinal and transverse for a transversely
490 isotropic model) from the central third of the bone. Longitudinal direction is defined as
491 the computed least-square line of the mesh nodes included in the bone diaphysis
492 surface.

493 Figure 4: Left: bending responses of the fourteen humeri. Right: bending stiffness of the
494 seven pairs of humeri, emphasizing the large inter- and intra-variability of measured
495 responses.

496 Figure 5. Bone meshes resulting from the reconstruction of segmented CT images
497 together with the mapping procedure. The colour code corresponds to the computed
498 densities (g/mm^3) assigned to each mesh element from HU values.

499 Figure 6. Left: experimental vs. simulated stiffness and yield load for the fourteen bone
500 samples and for the density-dependent transversely isotropic model. The dash line
501 represents a perfect prediction (simulation=experiments), whereas the continuous line
502 represents the linear fitting of the data. Right: Prediction error on stiffness and yield
503 load for the seven pairs of humeri.

504 Figure 7: Bland-Altman representation of the results obtained for the density-dependant
505 transversely isotropic model in terms of bending stiffness (left) and yield load (right).
506 Points are represented with the corresponding sample name (r=right, l=left).

507 Figure 8. Left: experimental vs. simulated stiffness and yield load for the fourteen bone
508 samples and for both a density-dependent transversely isotropic model and a density-
509 dependent isotropic model. Right: Prediction error on stiffness and yield load for these
510 two models.

511 Figure 9. Left: experimental vs. simulated stiffness and yield load for the fourteen bone
512 samples and for a two-material isotropic model. In this model, trabecular and cortical
513 tissues are considered homogeneous and are separated from density thresholds of

514 400HU or 600HU issued the CT-scan. Right: Prediction error on stiffness and yield load
515 for these two models.

516

517 **Table captions**

518 Table 1. Sensitivity analysis of the computational results : effect of resin properties,
519 spring stiffness and friction coefficient between bending stand and resin on predicted
520 bone stiffness and yield load. The star indicates a significant difference between a set of
521 parameters and the selected parameters in the presented simulations.

522 Table 2. Confrontation of the computational and experimental results in terms of
523 predicted yield load and bending stiffness. The p-value of ANOVA tests are given for
524 density-dependent transversely isotropic models (trans. iso), density-dependant
525 isotropic models (iso.) and two-materials isotropic models with segmentation threshold
526 of 400HU (400HU) and 600HU (600 HU). Low p-values indicate a significant difference
527 between experimental and simulation results.

528

Resin modulus (MPa)	Predicted Stiffness (N/mm)	Predicted yield load (N)	Spring stiffness (N/mm)	Predicted Stiffness (N/mm)	Predicted yield load (N)	Friction coefficient	Predicted Stiffness (N/mm)	Predicted yield load (N)
100	548.3	1500.2	1	532.3	1497.9	0.5	507.3	1425.9
500	548.3	1500.2	10	544.2	1500.1	0.6	527.2	1462.2
900	548.3	1500.2	100	548.8	1500.2	0.7	548.8	1500.2
1300	548.3	1500.2	1000	558.0	1489.4	0.8	572.2	1539.7
1700	548.3	1500.2	10000	544.0	1508.8	0.9	595.1	1590.8

529 Table 1 : Sensitivity analysis of the computational results : effect of resin properties, spring stiffness and
530 friction coefficient on predicted bone stiffness and yield load.

531

532

533

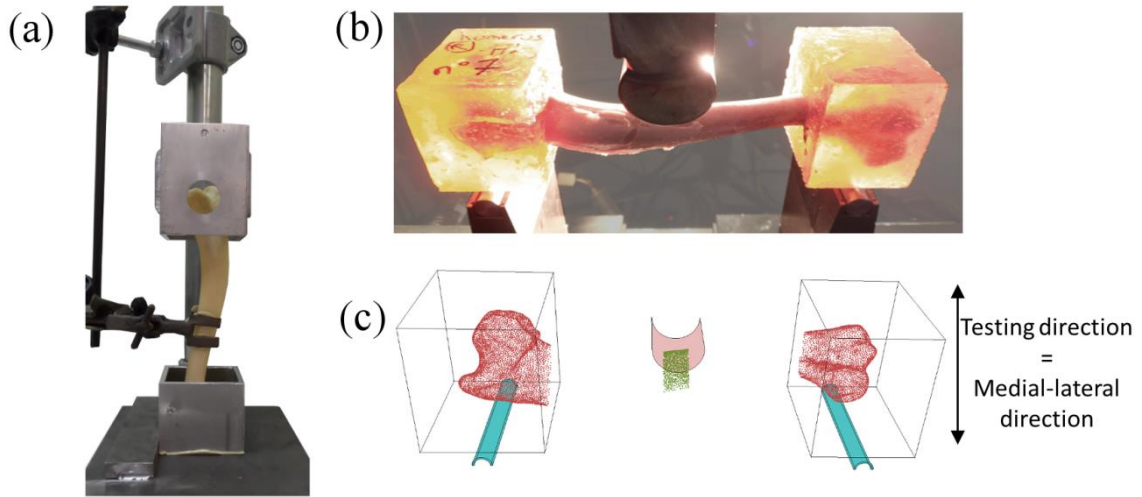
	Stiffness (N/mm)				Yield load (N)			
	Trans. Iso.	Iso.	400HU	600HU	Trans. Iso.	Iso.	400HU	600HU
<i>p-value</i> of the ANOVA test	0,67	2.48 10 ⁻⁴	0,43	0,17	0,74	4.13 10 ⁻⁵	0,18	0,08

534

535 Table 2: Confrontation of the computational and experimental results in terms of predicted yield load
536 and bending stiffness. The *p-value* of ANOVA tests are given for density-dependent transversely
537 isotropic models (trans. iso.), density-dependant isotropic models (iso.) and two-materials isotropic
538 models with segmentation threshold of 400HU (400HU) and 600HU (600 HU). Low *p-values* indicate a
539 significant difference between experimental and simulation results.

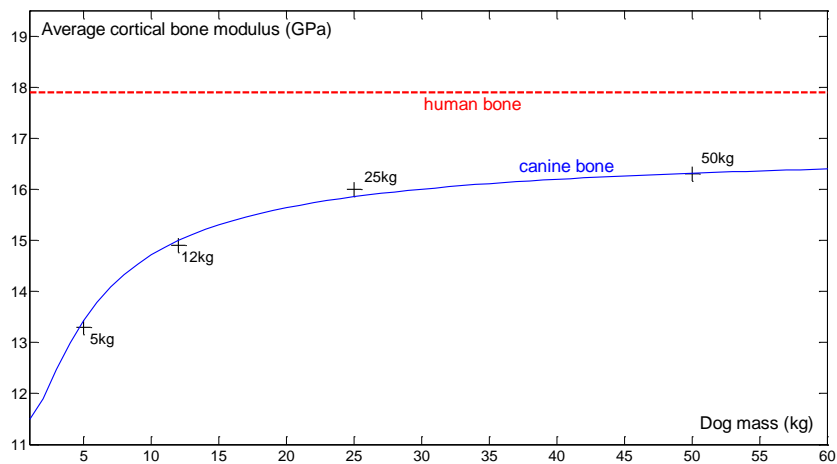
540

541



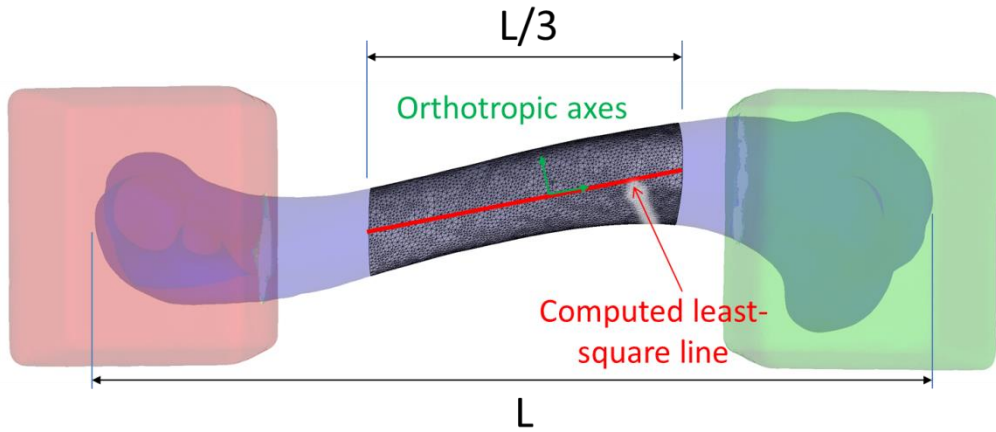
542
543
544
545
546
547
548
549

Figure 1: Experimental and simulated bending test on canine humerus. (a) Preparation of bone samples using a custom jig to align resin moulds (b) bone samples embedded in resin moulds were mounted in a custom bending stand (c) the bending tests were simulated by simplifying the resin moulds with single hexahedrons linked to the bone surface (red dots) via artificial springs. A sticking contact condition was considered between the bending tool and the bone surface (green dots), while contact-friction interaction was considered between the resin moulds and the bending stand (blue cylinders).



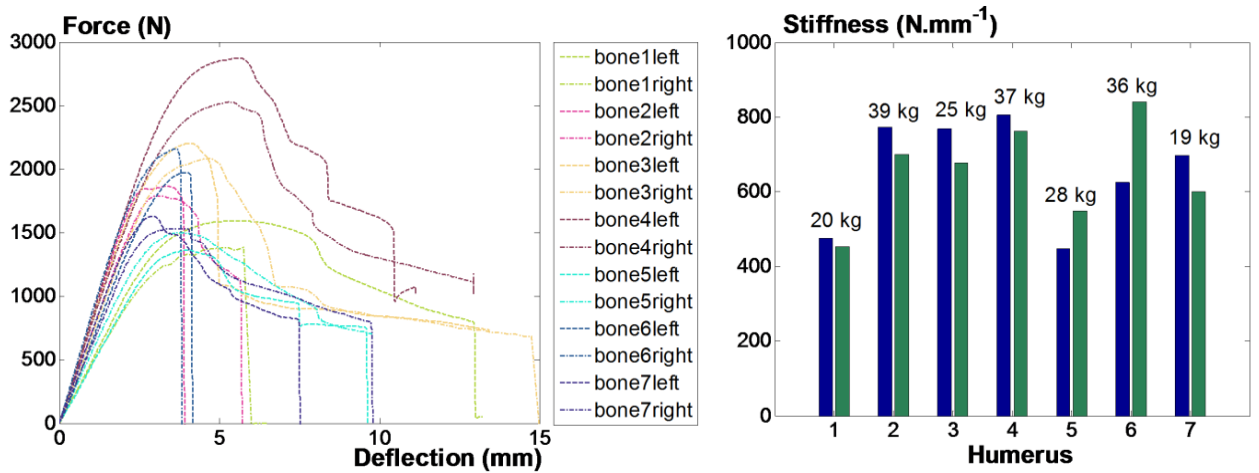
550
551
552
553

Figure 2. Determined relation between canine bone properties as a function of mass based on existing data¹⁹ and human bone properties.



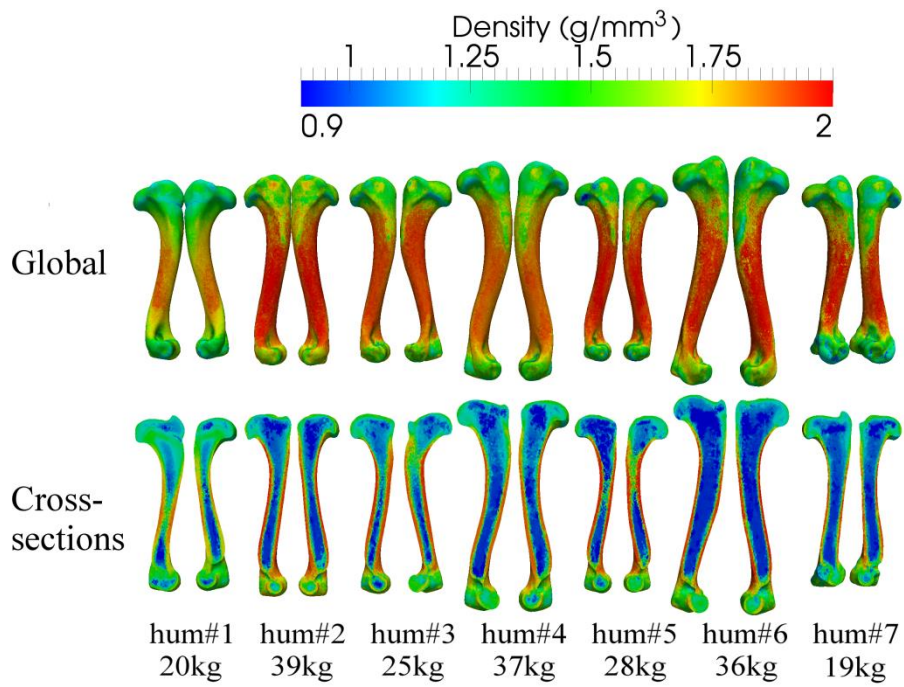
554
 555
 556
 557
 558
 559

Figure 3. Calculation of orthotropic axes (longitudinal and transverse for a transversely isotropic model) from the central third of the bone. Longitudinal direction is defined as the computed least-square line of the mesh nodes included in the bone diaphysis surface.



560
 561
 562

Figure 4: Left: bending responses of the fourteen humeri. Right: bending stiffness of the seven pairs of humeri, emphasizing the large inter- and intra-variability of measured responses.



563

564

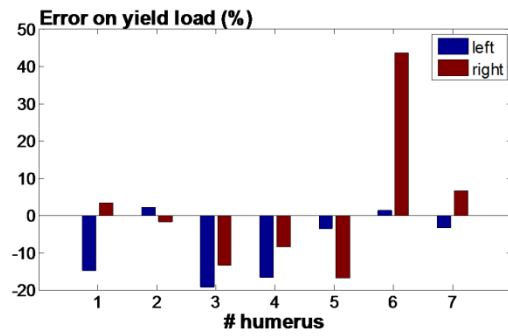
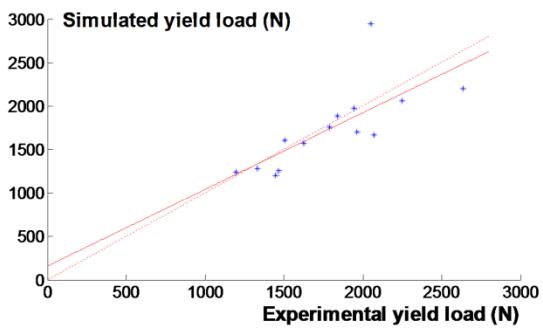
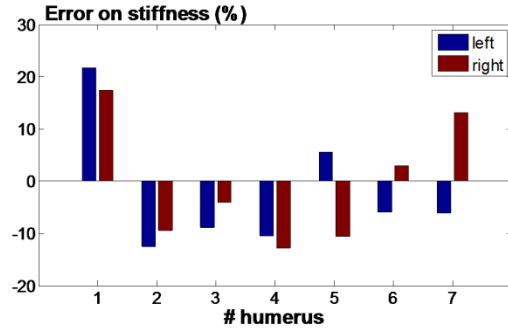
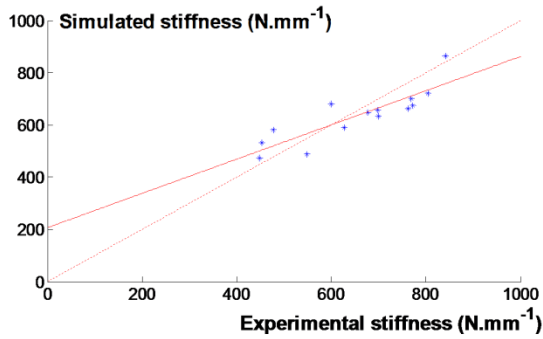
565

566

567

568

Figure 5. Bone meshes resulting from the reconstruction of segmented CT images together with the mapping procedure. The colour code corresponds to the computed densities (g/mm^3) assigned to each mesh element from HU values.



569

570

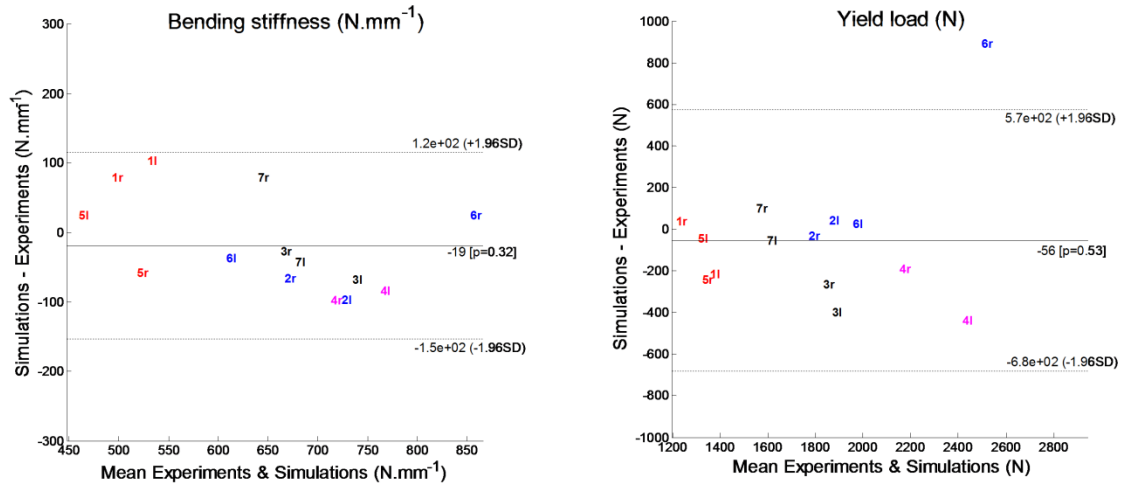
571

572

573

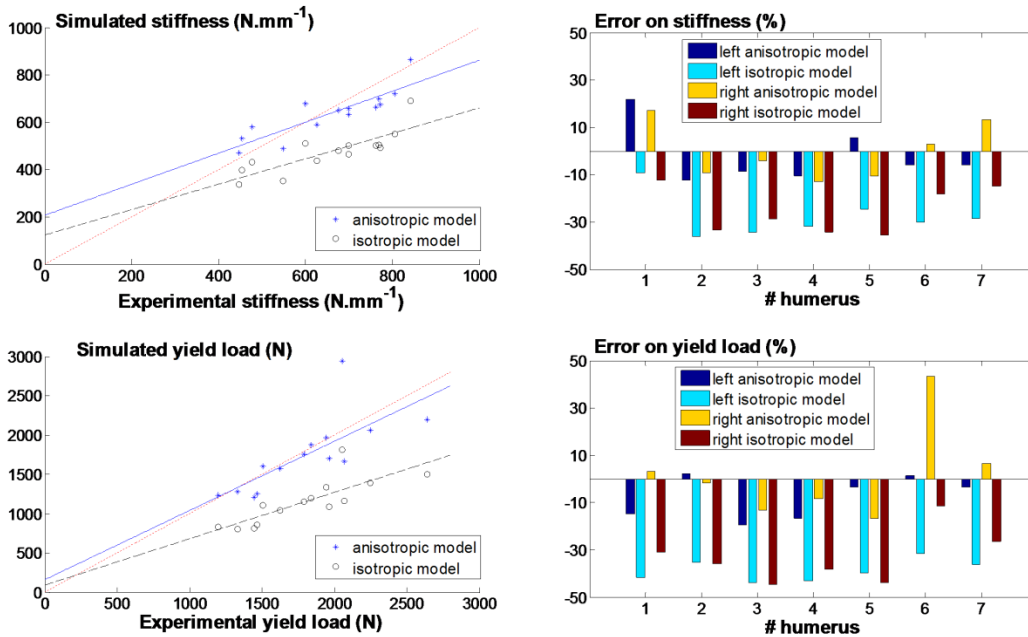
574

Figure 6. Left: experimental vs. simulated stiffness and yield load for the fourteen bone samples and for the density-dependent transversely isotropic model. The dash line represents a perfect prediction (simulation=experiments), whereas the continuous line represents the linear fitting of the data. Right: Prediction error on stiffness and yield load for the seven pairs of humeri.



575
576
577
578

Figure 7 : Bland-Altman representation of the results obtained for the density-dependant transversely isotropic model in terms of bending stiffness (left) and yield load (right). Points are represented with the corresponding sample name (r=right, l=left).

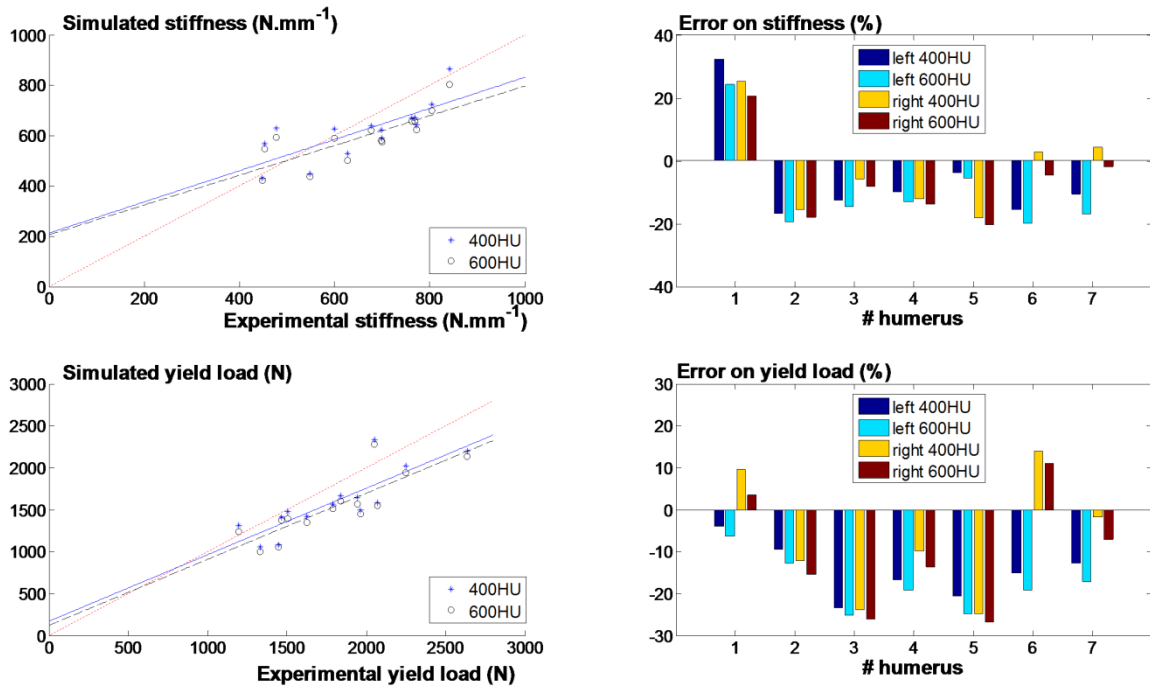


579
580
581
582
583

Figure 8. Left: experimental vs. simulated stiffness and yield load for the fourteen bone samples and for both a density-dependent transversely isotropic model and a density-dependent isotropic model. The red dash line represents a perfect prediction (simulation=experiments). Right: Prediction error on stiffness and yield load for these two models.

584

585



586

587

588

589

590

591

592

Figure 9. Left: experimental vs. simulated stiffness and yield load for the fourteen bone samples and for a two-material isotropic model. In this model, trabecular and cortical tissues are considered homogeneous and are separated from density thresholds of 400HU or 600HU issued the CT-scan. The red dash line represents a perfect prediction (simulation=experiments). Right: Prediction error on stiffness and yield load for these two models.